



# Terahertz polarimetry with a monolithic metasurface

THOMAS S. NOWACK,<sup>1,\*</sup>  YASH D. SHAH,<sup>2</sup>  IVONNE ESCORCIA,<sup>1</sup> JAMES P. GRANT,<sup>1</sup>   
MITCHELL KENNEY,<sup>1</sup>  VINCENZO PUSINO,<sup>1</sup>  DANIELE FACCIO,<sup>2</sup>  EDWARD WASIGE,<sup>1</sup> AND  
DAVID R. S. CUMMING<sup>1</sup>

<sup>1</sup>James Watt School of Engineering, University of Glasgow, Glasgow G12 8QQ, UK

<sup>2</sup>School of Physics and Astronomy, University of Glasgow, Glasgow G12 8QQ, UK

\*Corresponding author: thomas.nowack@glasgow.ac.uk

Received 6 May 2022; revised 2 June 2022; accepted 7 June 2022; posted 22 June 2022; published 12 August 2022

**The state of polarization (SoP) is a fundamental property of electromagnetic radiation that can carry a rich set of important information in light transmitted through a test sample. Despite a wide range of applications in material identification, (thin-film) characterization, and defect analysis, the SoP remains difficult to exploit—especially at terahertz frequencies since its measurement requires complex apparatuses with multiple moving parts. We have addressed these challenges by designing a metasurface polarimeter (MSP) that incorporates the entire functionality of a division of aperture polarimeter (DoAP) with high efficiency into a single silicon layer without the need for moving parts. Collective simulations are in perfect agreement with experimental data, both confirming the intended operation. Furthermore, we present an automated analysis algorithm that allows for the complete determination of the SoP from a single image with an experimental accuracy of  $92.1\% \pm 4.2\%$ , following an initial calibration. We anticipate that the presented MSP will find applications in polarimetric sensing and imaging for non-destructive evaluation at terahertz frequencies.**

Published by Optica Publishing Group under the terms of the [Creative Commons Attribution 4.0 License](https://creativecommons.org/licenses/by/4.0/). Further distribution of this work must maintain attribution to the author(s) and the published article's title, journal citation, and DOI.

<https://doi.org/10.1364/OL.463143>

The state of polarization (SoP) is a fundamental property of electromagnetic radiation that describes the time-averaged transverse oscillation of the electric field vector of a propagating wave. There are a wide range of polarization-dependent material interactions and polarizing effects that can be observed including diattenuation [1], birefringence [2], and Brewster's law [3]. The ability to measure the SoP accurately and quickly is of significance to a wide range of applications in material characterization such as ellipsometry [4], polarimetric imaging [5–7], and non-destructive testing [4,5].

The  $4 \times 1$  Stokes vector  $S$  with its parameters  $S_0$ – $S_3$  represents the most general description of the SoP and is commonly visualized on the Poincaré sphere [5]. Transitions between different SoPs can be achieved by introducing polarizing optics, which is commonly expressed using Mueller calculus [2]. Two important optical elements are the linear polarizer (LP) (ideally

with extinction ratio  $\cong \infty$ ) and the linear retarder with phase retardance  $\Delta$  [2].

Arbitrary polarization generators (APGs) for incident polarized light  $S_{in}$  can be built as a cascaded sequence of a rotatable half-wave retarder (HWR,  $\Delta = \pi$ ), a LP, and a quarter-wave retarder (QWR,  $\Delta = \pi/2$ ) [7]. This arrangement is valuable for polarimetry as it can generate any output polarization  $S_{out}$  as a function of both wave retarder's orientation angles  $\alpha$  and  $\beta$  according to Eq. (1) with the Mueller matrices  $M_i$  of each optical element  $i$  [2],

$$\vec{S}_{out} = \mathbf{M}_{QWR}(\beta) \cdot \mathbf{M}_{LP}(2\alpha) \cdot \mathbf{M}_{HWR}(\alpha) \cdot \vec{S}_{in}. \quad (1)$$

Polarization-analyzing instruments aim to determine the four Stokes parameters and require the quantitative measurement of at least four different SoPs that ideally form a tetrahedron within the Poincaré sphere (octahedron for six measurements) [5]. Traditional instruments based on classical components perform these measurements either sequentially (division of time) e.g., via the rotating QWR method, or in parallel e.g., using a division of aperture polarimeter (DoAP) [1]. Each method has drawbacks since sequential measurements are time-consuming and prone to errors arising from fluctuations between individual measurements, while parallel setups are typically complex, less efficient, and more expensive [1].

Metasurface-based polarimeters (MSPs) have considerable potential for ultra-fast measurements of the SoP in a single image. MSPs have recently been studied extensively to obtain improved performance, extreme compactness, and straightforward integrability at the system level [5,6,8–15]. Furthermore, polarimetric imaging has been shown for advanced designs, allowing for video-rate polarimetric inspection and characterization of large sample areas [5,6].

In this work, we present a MSP operating at terahertz frequencies that integrates the entire functionality of a DoAP into a single optical layer with high efficiency. Our design employed three sub-lattices that were interleaved throughout the entire active area of the metasurface. As a result, the intensity profile formed behind our MSP was invariant to transverse misalignments of the incident beam, rendering our MSP robust against these alignment errors, unlike earlier designs based on segmented aperture division [16–18]. Individually imposed phase functions for the six degenerate SoPs created a hexagonal set

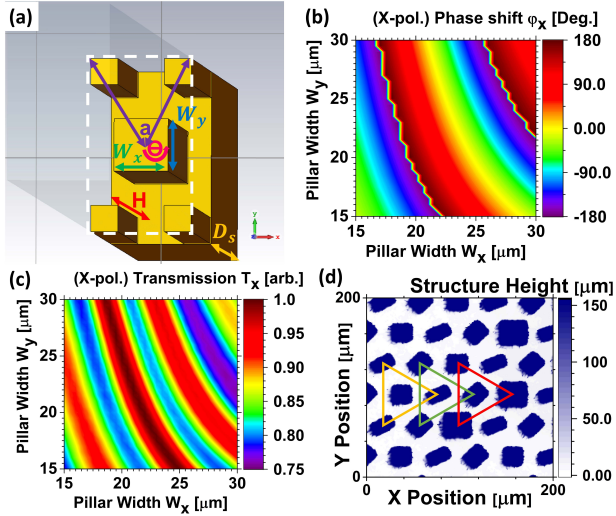


**Fig. 1.** (a) FDTD simulations of the unit cell (white dashed line) with its pillars, including highlighted design parameters. The nearest neighbor distance  $a = 40 \mu\text{m}$  and the pillar height of  $H = 150 \mu\text{m}$  are kept constant, whereas the pillar widths ( $W_x$ ,  $W_y$ ) and in-plane rotation angle  $\theta$  are varied in the range  $[15 \mu\text{m}, 30 \mu\text{m}]$  with  $0.5\text{-}\mu\text{m}$  step size and in steps of  $1^\circ$ , respectively. (b) Simulated phase shift  $\varphi_x$  and (c) transmission  $T_x$  for each pillar dimension for x-polarized light. (d) Surface profile of the fabricated metasurface obtained by optical interference profilometry showing the three triangular sub-lattices (colored triangles) and a uniform structure height of  $150 \mu\text{m}$ .

of focal points that were automatically analyzed using purpose-written software. The analysis script accounted for slight axial misalignment and thermally induced variations of the dark signal. The experimental measurement accuracy was  $92.1\% \pm 4.2\%$ .

The optimized unit cell of the dielectric metasurfaces was based on rectangular pillars with variable widths  $W_x$  and  $W_y$  that could be rotated in-plane by an angle  $\theta$ , as illustrated in Fig. 1 (a). At each lattice point, an algorithm used the simulation results shown in Figs. 1(b) and 1(c) in a look-up table to select the pillar dimensions that best approximated the polarization-dependent phase profiles described by Eq. (2), following an established routine for polarization-dependent phase encoding [8,19]. The monolithic metasurface design employed intrinsic silicon ( $>10,000 \Omega\text{cm}$ ) for both substrate and pillars due to its high refractive index ( $3.418$  [3]) with low dispersion [20] and a high transparency at the design wavelength  $\lambda_0$  of  $118.8 \mu\text{m}$ . The metasurface was fabricated in a single photolithographic step using SPR 220.7 photoresist followed by anisotropic dry-etch (Bosch process [21]) to form the pillars in bulk silicon. Figure 1(d) confirms a uniform etch depth of  $150 \mu\text{m}$ .

The design of the MSP divided the hexagonal arrangement of pillars into three sub-lattices with an individual nearest neighbor distance  $a_{\text{sub}}$  of  $69.3 \mu\text{m}$ , known as interleaved spatial multiplexing [17,18]. The pillars of each sub-lattice shown in Fig. 1(d) encoded a pair of independent phase functions on orthogonal SoPs that were linearly horizontal,  $\langle |H\rangle$ , and vertical,  $\langle |V\rangle$ , polarized (red triangle); linearly diagonal,  $\langle |D\rangle$ , and anti-diagonal,  $\langle |A\rangle$ , polarized (green triangle); and right,  $\langle |R\rangle$ , and left,  $\langle |L\rangle$ , circularly polarized (yellow triangle). Phase functions of spherical off-axis lenses  $\varphi_{1-6}(x, y)$  with the focal length  $f$  were chosen

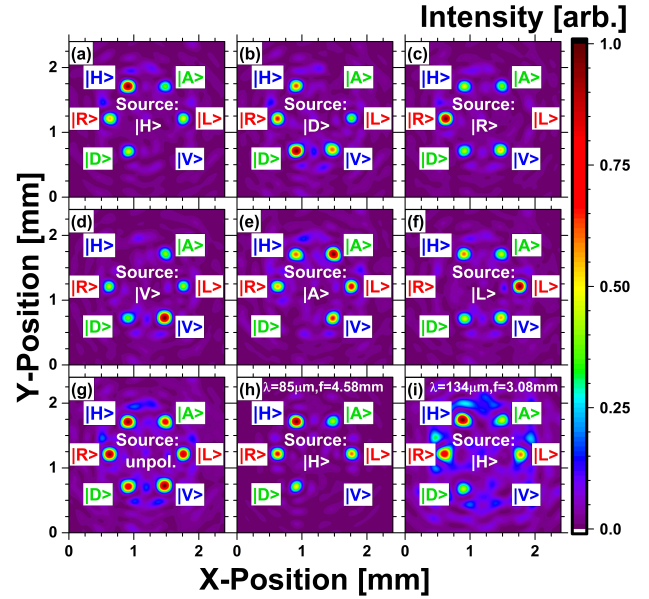


**Fig. 2.** Large area simulations of the MSP in Lumerical FDTD solutions for six incident SoPs: (a)  $\langle |H\rangle$ ; (b)  $\langle |D\rangle$ ; (c)  $\langle |R\rangle$ ; (d)  $\langle |V\rangle$ ; (e)  $\langle |A\rangle$ ; (f)  $\langle |L\rangle$ ; and (g) unpolarized light. Each image shows the transverse spatial distribution of the normalized intensity ( $E^2$ ) at the focal plane  $f = 3.2 \text{ mm}$  behind the metasurface. Stable operation was observed between (h)  $3.54 \text{ THz}$  and (i)  $2.24 \text{ THz}$ , albeit with a shifted focal length  $f$ . In each image, the focal spots originating from the six phase functions are labeled with their respective SoP with a designed off-axis displacement  $\Delta_{xy}$  of  $0.6 \text{ mm}$ . The intensity distribution between these six focal spots changes as function of the incident SoP.

for these six SoPs, see Eq. (2),

$$\varphi_{1-6}(\mathbf{x}, \mathbf{y}) = \frac{2\pi}{\lambda_0} \left( \mathbf{f} - \sqrt{[\mathbf{f}^2 + (\mathbf{x} - \mathbf{x}_0)^2 + (\mathbf{y} - \mathbf{y}_0)^2]} \right). \quad (2)$$

Each of these six phase functions  $\varphi_{1-6}$  generated one of the six differently polarized focal points observed in Fig. 2. The individual off-axis displacements  $\Delta_{xy} = |(x_0, y_0)|$  were chosen to arrange the six focal points at the vertices of a regular hexagon around the optical axis to ensure equal amounts of aberrations for every focal point.

Large area simulations of a scaled metasurface in Lumerical FDTD Solutions confirmed the intended operation of the MSP, as shown in Fig. 2. The intensity distribution between the six differently polarized focal points changed as a function of the SoP incident to the metasurface. For example, incident  $\langle |H\rangle$  polarized light in Fig. 2(a) resulted in equal intensities of the  $\langle |D\rangle$ ,  $\langle |A\rangle$ ,  $\langle |R\rangle$ , and  $\langle |L\rangle$  focal points, but a dominant  $\langle |H\rangle$  and absent  $\langle |V\rangle$  focal point. Unpolarized light led to all six focal spots excited with equal intensity in Fig. 2(g), which in principle also enables the analysis of partially polarized light. Preliminary broadband simulations that assumed negligibly small dispersion of silicon within the simulated spectral region [20] in Figs. 2(h) and 2(i) indicated a good operational bandwidth ( $\nu_{\text{opt}} = 2.52 \text{ THz}$ ) between approximately  $3.53 \text{ THz}$  and  $2.24 \text{ THz}$ , respectively, with a shifted focal plane due to negative chromatic aberration [22].

An analysis script and calibration measurements were necessary to calibrate the fabricated MSP prior to conducting

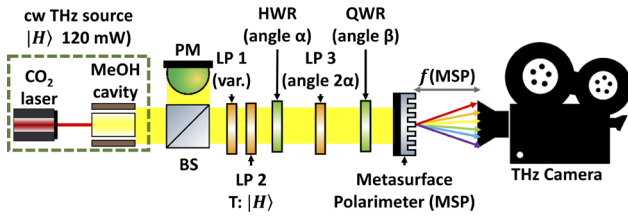


**Fig. 3.** Schematic of the setup employed for the calibration and SoP measurements. BS, non-polarizing beam splitter; PM, power meter; LP, linear polarizer; HWR/QWR, Half/Quarter wave retarder.

arbitrary SoP measurements [9,10,23]. The calibration required six images with incident light of the six degenerate SoPs. For each image  $k$ , the script located the peak positions of each focal point  $l$  and performed an individual background correction with a subsequent 2D-Gaussian fit to quantify the integrated intensities  $I(k, l)$  of the respective focal points. These integrated intensities were arranged within the  $6 \times 6$  intensity matrix  $I_C$ , while the respective Stokes vector  $S(k)$  of each image's incident SoP formed the columns of the  $4 \times 6$  Stokes matrix  $S_C$ . Finally, the  $6 \times 4$  calibration matrix  $C$  was generated in Eq. (3) with the pseudo-inverse of  $S_C$ ,

$$C = I_C \cdot \text{pinv}(S_C). \quad (3)$$

SoP measurements were conducted by obtaining the  $1 \times 6$  intensity vector  $I_m$  of an image with unknown SoP as described above for  $k = 1$ . The SoP was identified via its  $4 \times 1$  Stokes vector  $\vec{S}_m S_m$  according to Eq. (4),

$$\vec{S}_m = \text{pinv}(C) \cdot I_m. \quad (4)$$

The experimental setup for the calibration and measurement of the SoP is depicted in Fig. 3. The terahertz source (FIRL 295, Edinburgh Instruments) delivered a  $\langle |H\rangle$  polarized continuous-wave beam of up to 120 mW at 2.52 THz. A combination of a non-polarizing beam splitter and power meter created a reference arm to monitor power fluctuations via  $I_{\text{ref}}$  [10]. In the measurement arm, an initial pair of LPs allowed for dynamic adjustments of the beam intensity. The APG consisted of an HWR ( $\alpha$ ), LP ( $2\alpha$ ), and QWR ( $\beta$ ). The collimated beam incident on the MSP was split up into the hexagonal set of focal points 82 mm behind the MSP and imaged by the THz camera (INO MicroXCam-384-THz). Polarimetric images can be obtained in principle by placing the image sensor outside the focal plane as described in [5], but this was beyond the scope of this work.

The calibration measurements are depicted in Fig. 4 and show excellent agreement with the simulations in Fig. 2. An increasing dark signal can be observed throughout prolonged measurements as a consequence of heat generation from both the THz laser and image sensor, which was accounted for in our analysis script by including a background correction for each focal spot. An important benefit of the calibration methodology we used was that the potential non-uniformities of the sensor's spatial sensitivity were accounted for as well. As such, the systematically lower intensity detected at the sensor's right side e.g., the  $\langle |L\rangle$  focal point, compared to the  $\langle |H\rangle$  and  $\langle |D\rangle$  focal points in Fig. 4(f), was compensated in Eq. (3).

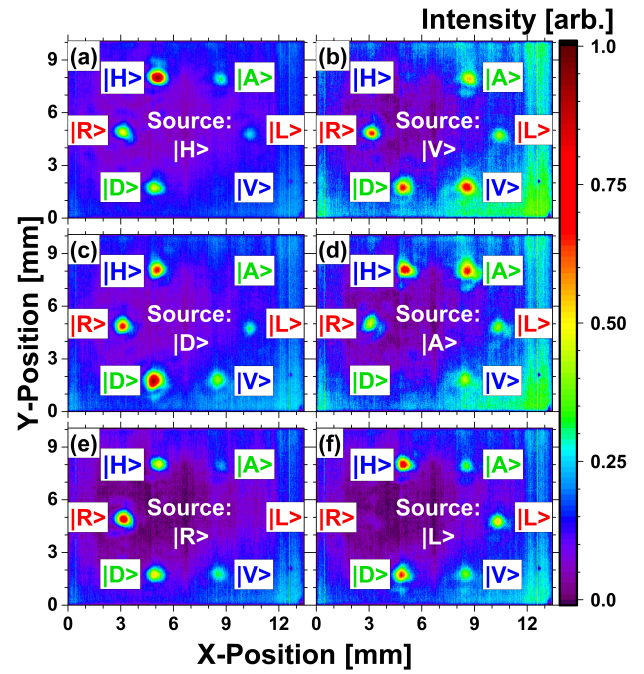


**Fig. 4.** Calibration measurements of the MSP with incident light of the six degenerate SoPs: (a)  $\langle |H\rangle$ ; (b)  $\langle |V\rangle$ ; (c)  $\langle |D\rangle$ ; (d)  $\langle |A\rangle$ ; (e)  $\langle |R\rangle$ ; and (f)  $\langle |L\rangle$ . Each image shows the detected intensity at the focal plane  $f = 82$  mm behind the metasurface. In each image, the focal spots originating from the six phase functions are labeled with their respective SoP with a designed off-axis displacement  $\Delta_{xy}$  of 3.88 mm. The intensity distribution between these six focal spots changes as a function of the incident SoP, in excellent agreement with the simulations in Fig. 2.

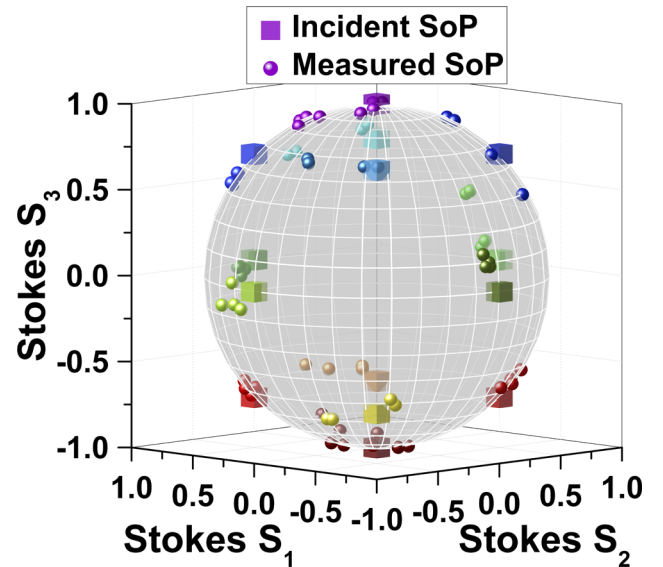


**Fig. 5.** Illustration of the Poincaré sphere showing the SoP incident on the metasurface calculated from the known orientation angles  $\alpha$  (HWR) and  $\beta$  (QWR) of the APG (14 colored cubes) compared to the SoP retrieved from the measurement images (64 respectively colored spherical markers) using the measurement methodology presented in this paper.

Figure 5 shows the known incident SoP as colored cubes on the Poincaré sphere with the SoP measurements as points of respective color. To quantify these results, we defined the measurement accuracy  $\eta_{\text{exp}}$  in Eq. (5) using the normalized orthodromic distance  $d_{\text{circ}}$  (radius = 1) between the theoretic (subscript t) and experimentally determined (subscript e) SoP in Eq. (6) with the azimuth angle  $2\Psi$  and latitude angle  $2\chi$ ,

$$\eta_{\text{exp}} = (1 - d_{\text{circ}}) \cdot 100 \%, \quad (5)$$

$$d_{\text{circ}} = \frac{1}{\pi} \text{acos}[\cos(2\Psi_t) \cos(2\Psi_e) \cos(2\chi_t - 2\chi_e) + \sin(2\Psi_t) \sin(2\Psi_e)] \quad (6)$$

The average measurement accuracy of all 64 measurements was  $92.1\% \pm 4.2\%$ , with a minimum value of 82.8%, which was in line with data in the literature for work at 800 nm [14] and 1550 nm [9]. Hence, the MSP presented in this work successfully measured the SoP at terahertz frequencies with high precision and repeatability, even compared to respective MSPs operating with more mature equipment at different wavelengths.

In conclusion, we have presented the design and experimental verification of a metasurface functioning as a DoAP at terahertz frequencies. The anisotropic meta-pillars were grouped into three interlaced sub-lattices that enabled the choice of independent phase functions for all six degenerate SoPs. The equidistant off-axis focusing of all six phase functions onto the vertices of a regular hexagon ensured approximately equal aberrations for each focal point. Interleaving the sub-lattices throughout the entire active area ensured operation that was invariant to small transverse misalignments of the metasurface. The intended operation was confirmed with large area simulations that were found to be in excellent agreement with experimental results.

To quantify the SoP from each individual image using the Stokes parameter, a calibration-based measurement methodology was developed and automated with a self-written analysis algorithm. The calibration took account of systematic error sources, such as increasing dark signal owing to uneven sensor heating, spatially varying pixel sensitivity, and slight axial misalignments of the metasurface. The SoP determined from the obtained images consistently agreed with the known SoP, with an experimentally obtained accuracy of  $92.1\% \pm 4.2\%$ . We expect the proposed MSP to be of considerable interest for applications in polarimetric terahertz imaging and sensing for non-destructive testing owing to the straight-forward integrability of the metasurface with an image sensor.

**Funding.** H2020 Marie Skłodowska-Curie Actions (765426, TeraApps); QuantIC (EP/T00097X/1).

**Acknowledgments.** The authors thank the staff of the James Watt Nanofabrication Centre for their support and Dr. Corrie Farmer for developing and optimizing fabrication and dry etch processes. This project has received funding from the European Union's Horizon 2020 research and innovation programme under the Marie Skłodowska-Curie grant agreement No. 765426 (TeraApps) and the UK Quantum Technology Hub in Quantum Imaging (EP/T00097X/1).

**Disclosures.** The authors declare no conflict of interest.

**Data availability.** Data underlying the results presented in this paper are available in Dataset 1.

## REFERENCES

- J. S. Tyo, D. L. Goldstein, D. B. Chenault, and J. A. Shaw, *Appl. Opt.* **45**, 5453 (2006).
- C. Lane, D. Rode, and T. Rosgen, *Appl. Opt.* **60**, 8435 (2021).
- S. Ding, Q. Li, R. Yao, and Q. Wang, *Appl. Phys. B* **98**, 119 (2010).
- Z. Mrzkova, M. Foldyna, S. Misra, M. Al-Ghazawat, K. Postava, J. Pištora, and P. Roca i Cabarrocas, *Appl. Surf. Sci.* **421**, 667 (2017).
- N. A. Rubin, G. D'Aversa, P. Chevalier, Z. Shi, W. T. Chen, and F. Capasso, *Science* **365**, eaax1839 (2019).
- E. Arbabi, S. M. Kamali, A. Arbabi, and A. Faraon, *ACS Photonics* **5**, 3132 (2018).
- Y. Dai, Y. Zhang, Y. Xie, D. Wang, X. Wang, T. Lei, C. Min, and X. Yuan, *Photonics Res.* **7**, 1066 (2019).
- J. P. Balthasar Mueller, N. A. Rubin, R. C. Devlin, B. Groever, and F. Capasso, *Phys. Rev. Lett.* **118**, 113901 (2017).
- Z. Yang, Z. Wang, Y. Wang, X. Feng, M. Zhao, Z. Wan, L. Zhu, J. Liu, Y. Huang, J. Xia, and M. Wegener, *Nat. Commun.* **9**, 4607 (2018).
- W. T. Chen, P. Torok, M. R. Foreman, C. Y. Liao, W. Y. Tsai, P. R. Wu, and D. P. Tsai, *Nanotechnology* **27**, 224002 (2016).
- A. Basiri, X. Chen, J. Bai, P. Amrollahi, J. Carpenter, Z. Holman, C. Wang, and Y. Yao, *Light: Sci. Appl.* **8**, 78 (2019).
- F. Ding, S. Tang, and S. I. Bozhevolnyi, *Adv. Photonics Res.* **2**, 2000173 (2021).
- F. Ding, A. Pors, Y. Chen, V. A. Zenin, and S. I. Bozhevolnyi, *ACS Photonics* **4**, 943 (2017).
- A. Pors, M. G. Nielsen, and S. I. Bozhevolnyi, *Optica* **2**, 716 (2015).
- L. Li, J. Wang, L. Kang, W. Liu, L. Yu, B. Zheng, M. L. Brongersma, D. H. Werner, S. Lan, Y. Shi, Y. Xu, and X. Wang, *ACS Nano* **14**, 16634 (2020).
- F. Ding, B. Chang, Q. Wei, L. Huang, X. Guan, and S. I. Bozhevolnyi, *Laser Photonics Rev.* **14**, 2000116 (2020).
- E. Arbabi, A. Arbabi, S. M. Kamali, Y. Horie, and A. Faraon, *Sci. Rep.* **6**, 32803 (2016).
- E. Maguid, I. Yulevich, D. Veksler, V. Kleiner, M. L. Brongersma, and E. Hasman, *Science* **352**, 1202 (2016).
- A. Arbabi, Y. Horie, M. Bagheri, and A. Faraon, *Nat. Nanotechnol.* **10**, 937 (2015).
- J. M. Dai, J. Q. Zhang, W. L. Zhang, and D. Grischkowsky, *J. Opt. Soc. Am. B* **21**, 1379 (2004).
- H. V. Jansen, M. J. de Boer, S. Unnikrishnan, M. C. Louwerse, and M. C. Elwenspoek, *J. Micromech. Microeng.* **19**, 033001 (2009).
- E. Arbabi, A. Arbabi, S. M. Kamali, Y. Horie, and A. Faraon, *Optica* **4**, 625 (2017).
- A. Cofré, A. Vargas, F. A. Torres-Ruiz, J. Campos, and A. Lizana, *Opt. Laser Technol.* **96**, 219 (2017).